A Polyextreme Hydrothermal System Controlled by Iron: The Case of Dallol at the Afar Triangle

Electra Kotopoulou,[†] Antonio Delgado Huertas,[†] Juan Manuel Garcia-Ruiz,*,[†] Jose M. Dominguez-Vera,[‡] Jose Maria Lopez-Garcia,[§] Isabel Guerra-Tschuschke,[∥] and Fernando Rull[⊥]

[†]Instituto Andaluz de Ciencias de la Tierra, (IACT), 18100 Granada, Spain
[‡]Departamento de Química Inorganica- Instituto de Biotecnologia, Universidad de Granada (UGR), 18071 Granada, Spain
[§]Instituto Geológico y Minero de España (IGME), 07006 Palma de Mallorca, Spain
[∥]Centro de Instrumentación Científica, Universidad de Granada (UGR), 18071 Granada, Spain
[⊥]Unidad Asociada UVa-CSIC al Centro de Astrobiología, University of Valladolid, 47002 Valladolid, Spain

S Supporting Information

ABSTRACT: One of the latest volcanic features of the Erta Ale range at the Afar Triangle (NE Ethiopia) has created a polyextreme hydrothermal system located at the Danakil depression on top of a protovolcano known as the dome of Dallol. The interaction of the underlying basaltic magma with the evaporitic salts of the Danakil depression has generated a unique, high-temperature (108 °C), hypersaline (NaCl supersaturated), hyperacidic (pH values from 0.1 to −1.7), oxygen-free hydrothermal site containing up to 150 g/L of iron. We find that the colorful brine pools and mineral patterns of Dallol derive from the slow oxygen diffusion and progressive oxidation of the dissolved ferrous iron, the iron-chlorine/-sulfate complexation, and the evaporation. These inorganic processes induce the precipitation of nanoscale jarosite-group minerals and iron(III)-oxyhydroxides over a vast deposition of halite displaying complex architectures. Our results suggest that life, if present under such conditions, does not play a dominant role in the geochemical cycling and mineral precipitation at Dallol as opposed to other hydrothermal sites. Dallol, a hydrothermal system controlled by iron, is a present-day laboratory for studying the precipitation and progressive oxidation of iron minerals, relevant for geochemical processes occurring at early Earth and Martian environments.

KEYWORDS: hyperacidic, hydrothermal, iron oxidation, Dallol, polyextreme, early Earth, Martian analogue-site

INTRODUCTION

The dome of Dallol lies in the Danakil depression at the extension of the Main Ethiopian Rift (MER) of the Afar Triangle (Figure 1a). This depression, situated 120 m below sea level (mbsl), is a vast salty plain composed of more than 2 km of evaporites created from successive marine transgressions of the Red Sea, the most recent placed at 32 kya, during the evolution of the MER since Miocene to Quaternary.[1] Categorized as BWh (hot desert climate) according to the Köppen classification[2] with scarce annual precipitation (up to 144 mm but usually below 50 mm) and a mean annual temperature of 35 °C,[2] the area of Danakil is one of the driest and hottest places on the planet. Danakil belongs to the dry drainage basin of Dinakle with no surficial flow and no, or insignificant, flow out of the drainage system.[3] However, the karstified Jurassic limestones and sandstones that underlay the evaporitic sequence behave as aquifers enabling the infiltration of meteoritic water from the Danakil Alps to the east and the highlands of the North Ethiopian plateau to the west, via the normal faulting and transverse fractures of the rift zone. In this

region of incipient seafloor spreading, where the crustal thickness does not exceed 14 km, the Red Sea, the Gulf of Aden, and the MER produce a triple junction zone associated with mantle plume activity and basaltic intrusive and extrusive magmatism.[4−7] As a result, several volcanic chains are forming, mainly represented by basaltic shield volcanoes, among them the NNW-SSE Erta Ale range. The Dallol dome along with the neighboring areas of the Black and Gaet' Ale Lakes (the latter also known as Yellow Lake)[8] are the most recent expressions at the northwestern part of the Erta Ale volcanic range; following from SE to NW the Hayli Gubbi, Ale Bagu, Erta Ale, Borale, Dalafilla, Alu, and Gada Ale volcanoes[9,10] (Figure 1a,b). The precise age of the Dallol dome is unknown, probably counting a few hundreds of years, whereas Black and Yellow lakes formed after the phreatic explosions of 1926 and 2005,
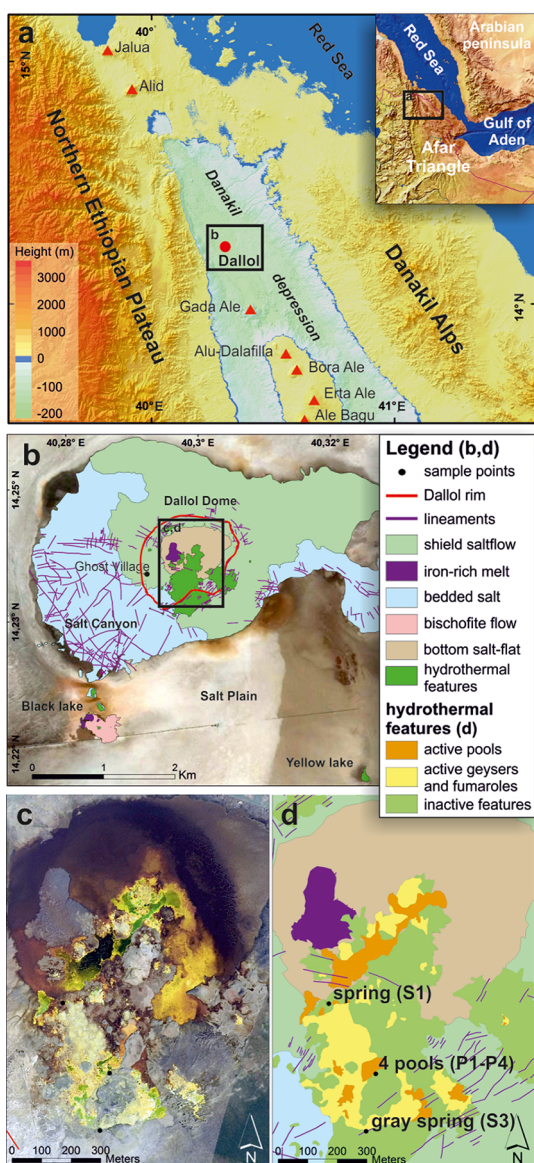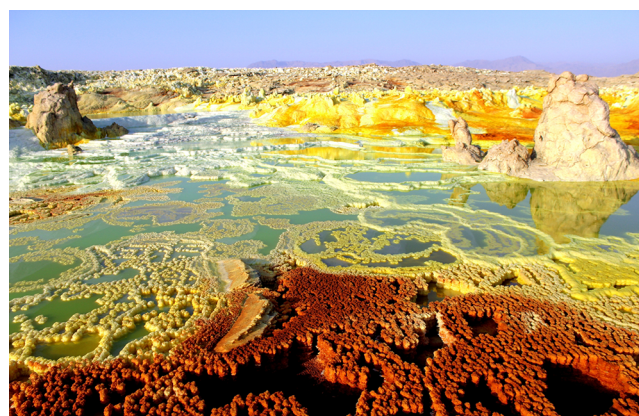
Figure 1. The hydrothermal system of Dallol within the Erta Ale range and maps of the active hydrothermal features of January 2017. (a) Dallol dome located in Danakil depression within the Erta Ale volcanic range of the Afar Triangle. (b) Geological map of the wider area of the Dallol dome, including Black and Yellow Lakes. (c) Aerial image of Dallol dome, showing the active areas in January 2017. (d) Map of January 2017 of the hydrothermal activity showing the referred sampling sites within the text, spring (S1), gray spring (S3) and a system of four successive pools (P1−P4).

respectively. Upwelling of basaltic magma confined in a magma chamber just 2.4 km deep below the segment of Dallol intruded the marine evaporitic sequence and created a dome structure lying 60 mbsl.[9,11,12] Dallol has not yet developed into a typical volcano; the ascending of magmatic fluids rich in CO_2, SO_2, H_2S and acidic gases, together with the boiling of meteoric water and of the seawater trapped in the evaporitic sequence, led to the generation of a hydrothermal system of hyperacidic springs with high content of dissolved CO_2 and chlorides.[9,11−13] This system is also characterized by an impressive palette of colors that is related to the high iron concentration of the fluids, deriving from the dissolution of the underlying basalt and iron-rich formations[14] (Figures 1 and 2).

In this work we unravel the geochemical processes of this singular geological site.

Figure 2. Representative image of the hydrothermal system of Dallol. Fumaroles and active hydrothermal chimneys forming terraces and pools are shown at the background of the image. Moving downward from the terraces, the oxidation of the Fe mineral precipitates is manifested by the change in the color from white to green, yellow, and finally to red. Pillars formed by exhausted springs of past hydrothermal activity are shown at the upper left and right of the image. The height of the right pillar is 1.5 m.

■ EXPERIMENTAL SECTION

In Situ Measurements. Temperature (± 0.1 °C) and pH (± 0.1) were measured, both for spring and pools, with a Hanna pH meter equipped with a glass electrode. Prior to the pH measurement the electrode was soaked in sulfuric acid (97.5%) for 24 h, whereas for the pH calibration we used buffers of pH 4, 2, 1.68, and 0.8. The pH meter was calibrated prior to every measurement and each measurement was repeated three times and in different days. Also, dissolved oxygen (μmol/L) was measured with the high sensitivity PreSens Fiber Optic Oxygen Meter Fibox 4, of temperature, automatic pressure and salinity compensation, and detection limit of 15 ppb dissolved oxygen, 0−100% oxygen. The PreSens system was calibrated with a two-point calibration before each measurement. Temperature, pH, and oxygen concentration measurements were repeated three times for the same sampling sites in different days during the fieldtrip.

Sampling and Preservation of the Anoxic Conditions. For the preservation of the pristine conditions of the liquids and to avoid the oxidation during the sample transportation and the measurements, samples of spring and pool water were collected in 12 mL sterile glass vials sealed with a septum tap, covered with parafilm tape and were kept inside a N_2 atm glovebox. Selected efflorescences and precipitates were preserved also in sterile glass septum sealed vials and in resealable with ziplock seal bags and were kept inside the glovebox. Bubbles of free gas were trapped within a plastic bucket with a pierceable tap. The gas was collected with a syringe and transferred to a 12 mL vial (Exetainer, Labco Limited, United Kingdom) previously filled with brine from the same sampling point. The gas displaces and replaces the brine until only a tiny residual liquid remains in the vial. Samples were collected in triplicate. For the analysis of dissolved gases, samples were stored in 12 mL vials with a pierceable tap (Exetainer, Labco Limited, United Kingdom).

The vials were filled as much as possible, avoiding bubbles. About 1 mg of mercury chloride was added to avoid biological activity.

Chemical Analysis of Water. Because of the high salinity of the brines, each sample within the 12 mL vials were diluted up to 50 mL and then they were filtered by 0.45 μm. For the determination of the concentration of the anion species we used a 940 Professional IC Vario instrument (Metrohm, Herisau, Switzerland) equipped with a conductivity detector at the Centro de Instrumentación Científica (CIC) of the University of Granada, Spain. An isocratic gradient of Na_2CO_3 (3.6 mM) was used as eluent, keeping an eluent flow at 0.7 mL min^{-1}. The injection loop was 50 μL. Analysis was done in an ionic resin column Metrosep A Supp 7−250/ 4.0. For the rest of the major, minor, and trace elements, samples were analyzed using an axial inductively coupled plasma optical emission spectrometer (axial ICP-OES Agilent (Varian) 720-ES). ICP analyses were carried out at the Instrumental Technical Services of the Estación Experimental del Zaidín (CSIC). Analytical quality control included analysis of one duplicate, three blank solutions, as well as analysis of a series of appropriate reference materials.

Raman and UV−vis Spectroscopy. Raman analysis of the pristine spring and pool water, preserved in oxygen-free conditions, was performed in the laboratory of the Espectrocopía Raman e Infrarroja aplicado a Cosmogeoquímica y Astrobiología (ERICA) of Unidad Asociada UVA-CSIC, Spain. Spectra were recorded with a Horiba-JY Induram spectrometer and a Laser Elforlight G4−30 PSU (532 nm) Cabezal Raman Horiba-JY Superhead, with a Zeiss 20× LF objetive. The laser potential was set at 20 mW and the water samples were placed vertically with respect to the beam. No sample preparation was required and the samples were not opened during the measurement.

For the investigation of the Fe aqueous species, we used the UNICAM UV300 spectrometer of the Inorganic Chemistry Department of the University of the Granada, Spain. Sample preparation was carried out inside a N_2 atm glovebox to preserve the oxygen-free conditions. Because of the very high amount of Fe in the liquids, a one-step dilution of 50 μL of sample into 1 mL of oxygen-free Milli-Q water was done prior to the measurement and samples were placed into quartz cells with septum seal. Spectra were recorded in absorbance mode, between 200 and 600 nm wavelengths, with a resolution of 1.5 nm. The (FZ) method used to determine Fe speciation in the liquids is detailed in the Supporting Information Methods 1.2.

Isotopic Analysis. Isotopic measurements were carried out in the Stable Isotope Laboratory of the Instituto Andaluz de Ciencias de la Tierra (CSIC-UGR, Granada, Spain). For the analysis of δD and $\delta^{18}O$ in water, an aliquot of water (0.7 μL) was injected onto a ceramic column containing a glassy carbon tube at 1450 °C to produce H_2 and CO gases.[15] A high-temperature reactor (TC/EA) coupled online via a ConFlo III interface to a Delta XP isotope ratio mass spectrometer (Thermo-Finnigan, Bremen). These gases were separated by chromatography using a helium carrier gas stream. To avoid memory effects, each sample was analyzed 10 times by discarding the first 5 analyses and averaging the last five. Commercial CO and H_2 bottles and five different waters, previously calibrated versus V-SMOW, SLAP, and GIPS, were used as internal standards for the oxygen and hydrogen isotopic analyses. The precision was calculated higher than 0.2 permil for the oxygen and 1 permil for the hydrogen, whereas the standard for reporting oxygen and hydrogen is V-SMOW (Vienna Standard Mean Ocean Water). The isotopic composition of nitrogen, carbon, and sulfur was analyzed by means of a Carlo Elba NC1500 (Milan, Italy) elemental analyzer with a Delta Plus XL (ThermoQuest, Bremen, Germany) mass spectrometer (EA-IRMS). Sulfur samples were mixed with vanadium pentoxide to ensure complete combustion. Internal standard previously calibrated vs IAEA-S1, IAEA-S2, IAEA-S3, NBS-127 y CP-1 for sulfur and NBS-22, IAEA-CH-7, IAEA-CH-6 for carbon were used. The methodology for the dissolved inorganic carbon (DIC) analysis is described in the Supporting Information Methods 1.2.

Dissolved Gases. For dissolved gas, a head space of 4 mL was created with ultrapure helium (99.9999) in the laboratory. The gases were analyzed in a continuous flow system that includes a liquid nitrogen trap, which prevents water vapor and CO_2 passing through the silica capilar, so that only a mixture of He (carrier), N_2, O_2 and Ar enters the spectrometer. The ratios O_2/Ar, N_2/Ar, CO_2/Ar, O_2/N_2 and isotopic composition of $^{15}N/^{14}N, ^{18}O/^{16}O, ^{17}O/^{16}O, ^{36}Ar/^{40}Ar, ^{38}Ar/^{40}Ar$ were analyzed with a mass spectrometer (Delta V plus; ThermoFinnigan, Bremen, Germany) that was specifically configured with 11 faraday cups to simultaneously analyze N_2, O_2, CO_2, and Ar. This allowed the maximum precision in the mixture of atmospheric gases. The precision was calculated for four bottles of internal standards versus air and was better than $\pm 0.03\%_o$ for $\delta^{15}N$, ± 0.05 $\delta^{17}O$, ± 0.02 $\delta^{18}O$, ± 0.06 $\delta^{36}Ar$, ± 0.1 $\delta^{38}Ar$, ± 0.8 for $\delta O_2/N_2$ (‰), ± 0.9 for $\delta O_2/Ar$ (‰), ± 0.56 for $\delta CO_2/Ar$ (‰). The methodology used for the in situ incubations is described in Supporting Information Methods 1.2.

High-Resolution Powder X-ray Diffraction (HRPXRD). For the detection of the crystalline phases of the mineral precipitates we used a high-resolution Bruker D8 Advance Series II X-ray diffractometer using monochromatic Cu K$_{\alpha 1}$ radiation with a primary Ge(111) monochromator and a PSD Lynxeye detector at the facilities of the Laboratorio de Estudios Crystalográficos (LEC) of the Instituto Andaluz de Ciencias de la Tierra (IACT) in Granada, Spain. Samples were run in transmission mode, at 40 kV acceleration voltage, and at 40 mA current for 16 h from 4° to 90° 2θ, 0.014° per second. Phase identification was carried out with the Diffrac.Suite software and the American Mineralogist Crystal Structure Database.

Field Emission Gun Scanning Electron Microscopy (FESEM-EDS). A ZEISS SUPRA 40 VP, FESEM-EDS equipped with an Oxford energy-dispersive X-ray spectrometer (EDS) of the Centro de Instrumentación Científica (CIC) of the University of Granada, Spain, operating at 5−20 keV was used for the textural and chemical characterization of the submicron mineral phases. High-resolution images were obtained at 5 kV and at 2 mm working distance, in SE and 15 kV in BS mode, whereas for the elemental analyses operating conditions were set at 15 kV accelerating voltage and 7.5 mm working distance and the AZtec 3.0 SP1 EDS software was used. Biological sample preparation for the SEM study is specified in the Supporting Information Methods 1.3.

Micro-Raman. The micro-Raman study of the solids was performed in the laboratory of the Espectroscopía Raman e Infrarroja aplicado a Cosmogeoquímica y Astrobiología (ERICA) of the Unidad Asociada UVA-CSIC, Spain. The spectra were obtained with a Kaiser OSI HoloSpec f/1.8i.

CCD Andor DV420A-OE-130 spectrometer equipped with a Research Electro-Optics LSRP-3501, He−Ne 632.8 nm laser, and a Cabezal Raman Kaiser OSI MKII, HFPH-FC-S-632.8 with a Nikon Eclipse E600 microscope with Nikon 50× by 100× LF objectives. The spot size was 38 μm for the 50× objective and 15 μm for the 100× objective.

Transmission Electron Microscopy. The study in the nanoscale was performed with a Titan X-FEG G2-S/TEM, image C_s-corrector, operating at a 300 kV acceleration voltage at the Centro de Instrumentación Científica (CIC) of the University of Granada, Spain. Samples were placed on a Formvar C coated Cu-grid. Z-contrast images were collected using a high-angle annular dark-field (HADDF) detector in scanning transmission mode (STEM), whereas the chemical composition of the studied phases was obtained with EDX. Also, high-resolution transmission electron microscopy (HRTEM), along with fast fourier transform images (FFT), and selected area electron diffraction (SAED) were performed to investigate the crystal structure of the studied nanophases.

■ RESULTS AND DISCUSSION

A Highly Active, Polyextreme Hydrothermal System. The crater of the Dallol dome hosts numerous springs, extended fumarolic fields, subaerial and subaqueous hydrothermal springs, and acidic brines that produce salt chimneys, pillars, terraces, and pools of different ephemeral colors (Figure 2). The hydrothermal system is highly dynamic; active spring sites go inactive and new springs emerge in new locations in the range of days, while the activity is changing in the range of hours within the same site. Eleven spring sites occupying an area of 0.038 km² were active in 2016, whereas 18 spring sites covering a 0.144 km² area where active in 2017, along NNE trending fissures (see Figure 1B and Supporting Information Figure S-1). However, the dominant geochemical characteristics of the system remained within a narrow range of values between the two field campaigns. The springs are discharging oxygen-free, hyperacidic, Fe-rich hydrothermal brines, which are supersaturated with respect to halite as soon as they are in contact with the atmosphere. The mean concentrations of the major elements of the spring brines are Cl (251.4 g/L) and Na (92.2 g/L) followed by Fe (22.5 g/L), K (10 g/L), S (3.6 g/L, measured as sulfate), Mg (3.7 g/L), and Ca (2.7 g/L), whereas the most abundant trace elements are Mn (714 ppm), F (302 ppm), Br (288 ppm), Al (279 ppm), and Zn (54 ppm) (see Supporting Information Table S-1). The composition of the gases emitted from the fumarolic fields and the spring complexes of Dallol is dominated by CO_2 (ranging from 70 to 99%) along with H_2S, N_2, and traces of H_2, Ar, and O_2 (Table S-2).[13]

The temperature of the spring water varies between 105.6 (±0.1) °C and 108.4 (±0.1) °C. Upon discharge, the water from the brines evaporates and the pressure and temperature decrease abruptly, triggering almost instantaneous precipitation of halite, creating pillars up to few meters in height. As the water flows downstream from the springs, a series of self-organized halite terraces pool the brines, which reduces turbulent flow. The temperature of the upper pools, those closest to the spring, is 85−71 (±0.1) °C, whereas it drops down to 32 (±0.1) °C due to increasing equilibration time with the atmosphere and evaporative cooling. The pH values of the spring water are close to zero ranging from 0.16 to −0.5 (±0.1). These hyperacidic values decrease from the upper to the lower pools, the lowest pH value measured in both field

missions was −1.7 (±0.1) (Table S-1). Hyperacidic values have been reported as well for several volcanic crater lakes and hot springs, among them the Kawah Ijen crater lake in Indonesia (pH ∼ 0.3),[16] the Poas crater in Costa Rica (pH ∼ −0.89),[17,18] the Ebeco Volcano in Kuril Islands (pH ∼ 0.2)[19] the Copahue in Argentina (pH ∼ 0.2),[20−22] the Ruapehu in New Zealand (pH ∼ 0.6),[23] the Nevado del Ruiz, Colombia (pH ∼ 1),[24] and the Santa Ana Volcano, El Salvador (pH ∼ 0.5).[25] Concerning acid mine effluents, hyper-acidic to acidic pH values (0.9−3) have been measured in Rio Tinto in Spain,[26] while[27] reporting a bizarre much lower value of pH, −3.6, from the Richmond Mine of the Iron Mt in California. Thus, to the best of our knowledge, the hydrothermal system of Dallol is the most acidic natural system.

Figure 3 shows the main acidic components of Dallol (sulfates, chlorides, fluorides, and dissolved iron) in compar-
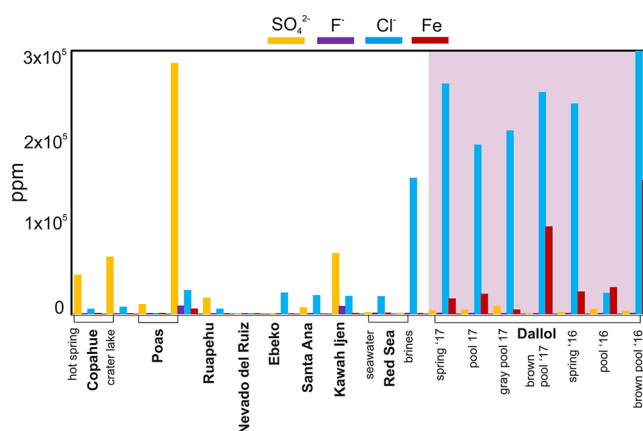

Figure 3. Comparative bar graph of sulfate, chloride, fluoride, and iron concentrations of Dallol (purple-shaded area) and other hyperacidic volcanic sites and the Red Sea brines. The values for Copahue,[22] Poas,[17,18] Ruapehu,[23] Nevado del Ruiz,[24] Ebeko,[19] Santa Ana,[25] Kawah Ijen,[16] Red Sea brines,[28] and Dallol (this study) acidic fluids are shown in ppm.

ison with those of other hyperacidic volcano-hydrothermal systems. Dallol fluids exhibit positive anomalies in chlorides (>200 g/L), derived from the interaction of ascending magmatic fluids rich in acidic gases (e.g., HCl(g), HF(g)) with the marine evaporites (containing halite, sylvite, carnallite, gypsum, anhydrite) and in dissolved iron originated from the interaction of the fluids with the underlain basalts and Fe-rich formations. The sulfate values (∼5200 ppm) are lower than the mean values of other volcano-hydrothermal systems, whereas the mean fluoride concentration (∼252 ppm) is comparable to the concentration of the other systems. Consequently, the hyper-acidic pH of the Dallol spring water (pH ∼ 0) results from the presence of strong acids and the formation of Fe(II)-chloro-complexes/-sulfates that are favored in these conditions of which the gradual oxidation and concentration in the hydrothermal pools decreases further the pH down to negative values.

Unlike the Dallol hydrothermal brines, neighboring Black Lake is a magnesium chloride pond of 2.5 (±0.1) pH and 60 °C (±0.1) temperature, whereas Yellow Lake is mainly composed of calcium chloride along with magnesium and potassium chlorides of 1.7 (±0.1) pH and 38 °C (±0.1) temperature (Figure 1b and Table S-1). The surrounding area of the salt plain, composed of Na/Ca-K/Mg/Fe-salts and

-sulfates, and clays[29] had a pH of 3.5 (± 0.1) when flooded with perennial water.

The Color Palette of Dallol. One of the most striking features of Dallol is the broad palette of colors of the brines and the solids, controlled by the iron redox chemistry. Because of the near zero pH of the spring water and the low dissociation constants of hydrogen sulfide,[30,31] the concentration of sulfide in the fluid is practically zero. Sulfur is mainly found around the fumarolic sites as millimeter-to centimeter dull yellow spheroids made of colloidal and poorly crystalline sulfur formed through atmospheric hydrogen sulfide oxidation. On the other hand, sulfates are present in the brines due to the dissolution of the sulfate salts of the evaporitic sequence. Therefore, the aqueous chemistry and the color palette of Dallol should be dominated by the formation of different iron species in both reduced and oxidized states.[32] To determine the redox state across the aqueous system of Dallol, we quantified the concentration of Fe(II) and Fe(III) in different spring solutions and related pools. Fe(II) concentration was determined by employing the external chelator ferrozine and by using UV−vis spectroscopy, Fe(Tot) was measured by ICP-MS/OES, and Fe(III) was obtained as the difference (Figure 4
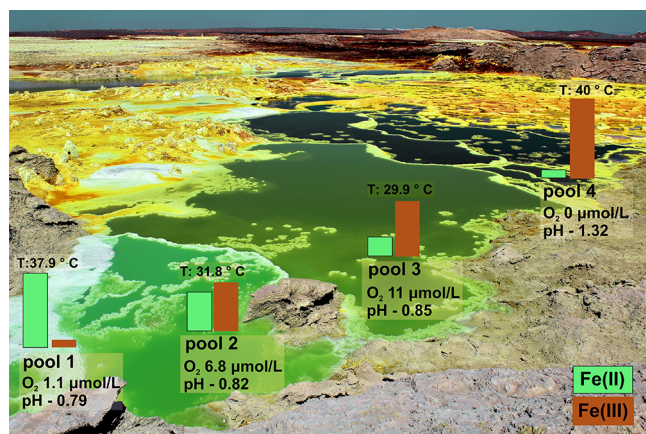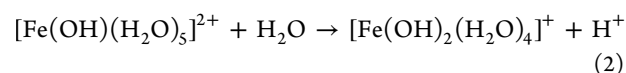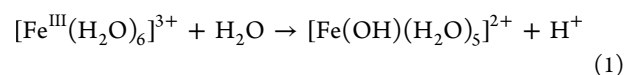

Figure 4. Fe(II)/Fe(III) ratio, pH, O$_2$ concentration, and temperature of four successive pools of a typical spring-terrace system. Pool 1 (P1), the upper pool (oxygen-free spring is at the left of the pool, out of the field of view), is dominated by Fe(II) species of light green color. Moving downstream from the spring to pool 3 (P3), temperature is decreasing and the atmospheric O$_2$ diffusion results to the formation of Fe(III) species and to pH drop. Ultimately, the lowest pool 4 (P4) is characterized by Fe(III), the precipitation of which darkens the color of the pool, lowers further the pH, increases the temperature, and consumes the oxygen.

and Supporting Information Methods 1.1. and Figure S-2). The measured values show that Fe(Tot) is practically ferrous in the spring water and is gradually oxidized to the pools until is completely converted to ferric iron in the lowest most concentrated pools (Figure 4 and Figure S-2). This gradual oxidation of the Fe(II) is reflected in both the pH and the color of the pools. The pH decreases from −0.79 (± 0.1) in pool 1 to −1.32 (± 0.1) in pool 4 followed by a change in the color of the pools from light green to dark brown due to hydrolysis and concentrative evaporation of the Fe(III) species that release further H$^+$. However, the heat produced by the exothermic Fe(II) oxidation and the increase in the thermal energy by light absorption in the dark brown color pools are responsible for the increase in temperature from 32 (± 0.1) °C

in pool 3 to 40 (± 0.1) °C in pool 4. The high consumption rate of oxygen due to oxidation of the Fe(II) and the precipitation of the Fe(III) minerals explains the anoxic conditions in the lowest pools of the hydrothermal field (Figure 4, pool 4).

We used Raman and UV−vis spectroscopies to identify the Fe aqueous species responsible for the colors of the pools. The light green color of the spring and upper pools is due to ferrous species, mainly associated with the v1(A1) (Fe−OH$_2$) stretching band at 370 cm^{-1} of the [Fe^{II}(H$_2$O)$_6$]$^{2+}$ and the broad band around 420−480 cm^{-1}, although, in this region there is an overlap with the deformation modes of the sulfate/bisulfate anions (Figure 5a, spring and pool 1).[33,34] Moving from the upper to the lower pools, the [Fe^{II}(H$_2$O)$_6$]$^{2+}$ is oxidized and the hexaquairon complex [Fe^{III}(H$_2$O)$_6$]$^{3+}$ undergoes hydrolysis to form progressive hydroxo-species, namely [Fe(OH)(H$_2$O)$_5$]$^{2+}$ and [Fe(OH)$_2$(H$_2$O)$_4$]$^+$ with the accompanying pH drop (eqs 1 and 2)

$$[\text{Fe}^{III}(\text{H}_2\text{O})_6]^{3+} + \text{H}_2\text{O} \rightarrow [\text{Fe(OH)}(\text{H}_2\text{O})_5]^{2+} + \text{H}^+ \tag{1}$$

$$[\text{Fe(OH)}(\text{H}_2\text{O})_5]^{2+} + \text{H}_2\text{O} \rightarrow [\text{Fe(OH)}_2(\text{H}_2\text{O})_4]^+ + \text{H}^+ \tag{2}$$

Furthermore, the very low pH and the high chloride concentration of the brines favor the formation of a complex mixture of Fe(III)-chlorides, such as [FeCl$_2$(H$_2$O)$_5$]$^{2+}$ and [FeCl$_2$(H$_2$O)$_4$]$^+$.[32,35,36] The latter is the most abundant and was identified by the 312 cm^{-1} band arising from the v (Fe^{3+}-Cl) stretching vibration in the spectra of the middle and lower pools[37] (Figure 5a). Note that the intensity of the band at 312 cm^{-1} is increasing from pool 2 to pool 4 as the concentration of Fe(III) is increasing, whereas the 370 cm^{-1} band decreases dramatically as the Fe(II) species decrease (Figure 5a). Likewise, the intensity of the v1(A1) vibration of the free SO$_4$$^{2-}$ at 982 cm^{-1} is decreasing from the spring water to pool 4 and equilibrates with the v(HO-S) and the SO$_3$ vibrations of the bisulfate anion at 875 and at 1052 cm^{-1}, respectively (Figure 5a, pools 3 and 4).[33,34] The UV−vis spectra of springs and pools consist of a broad absorption band centered around 330 nm that becomes more intense as we move from the spring to pool 4 (Figure 5b).

The major electronic transitions for the Fe(III) hydroxo- and chloro-complexes are attributed to ligand-to-metal charge transfers (LMCT). The LMCT absorption of the hydroxo-complexes occurs around 300 nm, whereas in the chloride-complexes this absorption intensifies and shifts to lower energies up to 360 nm.[36] Therefore, and in accordance with the Raman study, the UV−vis spectra show that the Fe(III)-chlorides are practically absent in the spring and the upper pools and become predominant in the lower pools, which explains the intense yellow color. Finally, the lowest pools show darker color due to further oxidation that provokes the precipitation of hydrated yellow iron-oxyhydroxides/-oxides/-sulfates. Two main mineral phases have been identified by X-ray diffraction, Raman spectroscopy, field emission scanning electron microscopy and energy-dispersive analysis, transmission electron microscopy, and diffraction: jarosite (KFe^{3+}$_3$(SO$_4$)$_2$(OH)$_6$) and akaganeite (β-Fe^{3+}O(OH,Cl)), products of the Fe(III) hydrolysis in the presence of sulfate and chloride, respectively.

Mineral Patterns. Regarding the solids halite is the dominant macrocrystalline phase found all over the Dallol
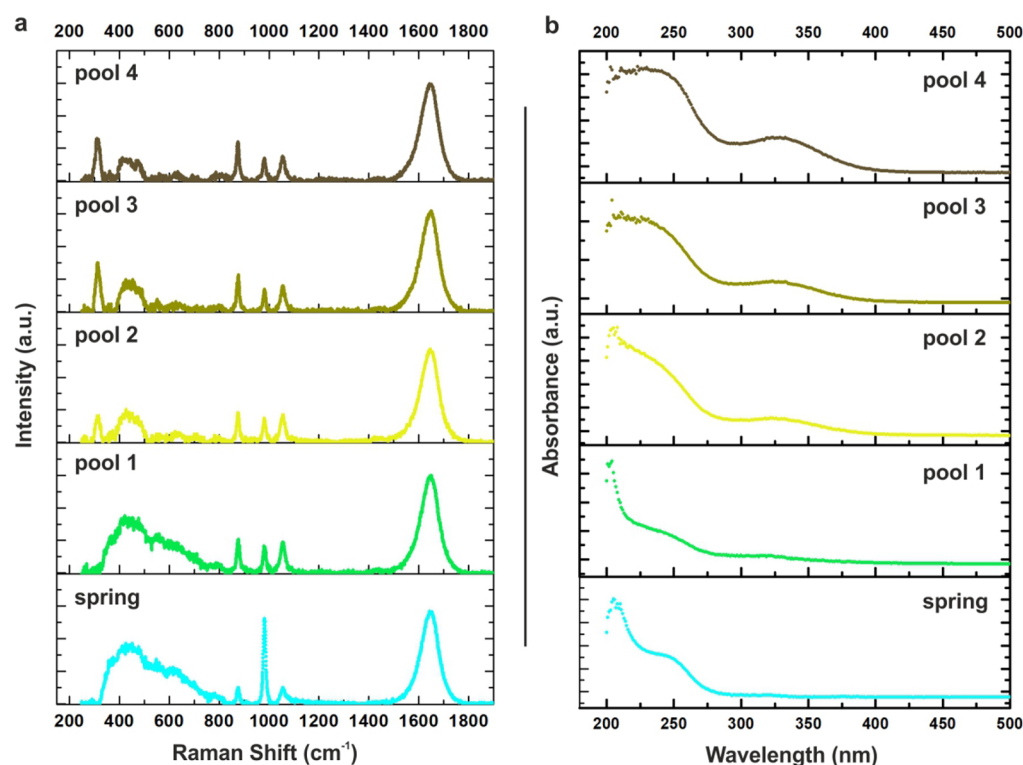
Figure 5. Raman and UV−vis spectra of the spring water (S1) and the four gradual pools (P1−P4) of Figure 1 and Figure 4. (a) Region of the Raman spectra showing the main vibrations of the Fe aqueous complexes. The concentration of the Fe(III) is increasing gradually from pool 2 to pool 4, as shown by the Fe(III)-Cl stretching vibration band at 312 cm^{-1}. This correlates with the decrease of the intensity of the Fe(II)−OH$_2$ stretching vibration at 370 cm^{-1}. (b) UV-absorbance spectra showing the increase of the band centered at 330 nm from the spring and upper pool to the lowest pools, due to Fe(II) oxidation and Cl-complexation.

dome, producing an impressive array of complex mineral patterns (Figure 6). Among them we underline the following: (i) hydrothermal salt-pillars up to 4 m high, (ii) water-lily structures forming in subaqueous springs, (iii) flower-like crystals growing in lower pools by extreme evaporation, (iv) egg-shaped thin crusts, hollow twisted tubes, and pearl-like spheres around active gas gateways, (v) various types of efflorescences, and (vi) polygonal cracking patterns resembling pieces in a chocolate bar (Figure 6). Salt pillars and water lilies form by subaerial and subaqueous halite crystallization, respectively, due to the cooling of the supersaturated brines. Evaporation and evaporative cooling drive the crystallization of the aforementioned structures except for the "chocolate bar" polygonal cracks, probably formed due to cooling stress, water loss, and solidification of a highly viscous sodium chloride, Fe-rich, solution. On top of the halite crystals, microcrystals of Na-/K-/Ca-/Mg-salts, such as, gypsum (CaSO$_4$·2H$_2$O), sodium-sulfates, sylvite (KCl), and carnallite (KMgCl$_3$·6H$_2$O) are precipitating. Nevertheless, the minor phases of submicrometer Fe-(oxy)hydroxides/sulfates, mainly jarosite (KFe^{3+}$_3$(SO$_4$)$_2$(OH)$_6$) and akaganeite (β-Fe^{3+}O(OH,Cl) that form a colorful veil over all the mineral patterns, are those responsible for the color diversity and color evolution of the solids with time (Figure 6h−m). Far from the active springs and their corresponding pools, the predominant phases are the Fe-oxides mainly represented by hematite (Fe$_2$O$_3$) (Figure 6i−m). Raman scattering from the precipitates did not pick up any organic compounds related to biologic activity, such as bacterial pigments (e.g., carotenoids, chlorophyll) that would produce a set of bands in the region 1000−1600 cm^{-1} and would affect their color.[38,39] Therefore, the color of the solids

starts as white around the springs due to the rapid halite crystallization with fluid inclusions but turns to yellowish and then to orange and brown as the Fe-oxidation, evaporation, and precipitation of jarosite, akaganeite, hematite, and other Fe-oxides takes place as aforementioned. Following aggregation of the Fe-particles, the color intensity is increased to a dark-red, brown-purple color. In addition to the sulfur spheroids mentioned above, few nanoparticles of S° and Fe-sulfides were also found dispersed in halite crystals probably deriving from the reduction of Fe(III) trapped in the halite crystals by the hydrogen sulfide gas.

In contrast to other hydrothermal systems, such as Yellowstone, where the color is clearly associated with microbial biofilms,[40] the entire color palette of Dallol is the result of inorganic processes. This gradual color variation, ranging from pale green to dark brown and reds, is beautifully displayed in Dallol due to the combined action of the continuous discharge of oxygen-free Fe(II)-rich spring brines, the low solubility of oxygen in high temperature, hyperacidic, and hypersaline brines, and therefore the slow oxidation of the Fe(II) species. The prevalence of laminar flow in the terrace-pool system and the dominance of diffusion over convection along the entire aqueous pathway from the springs to the pools slow down the dynamics of the system, enabling the discrete display of the stunning colors.

Isotopic Study. Dallol spring water has δD values similar to the local meteoric water (−21‰ to −8 ‰ versus V-SMOW),[41,42] while the δ^{18}O values of the spring water are shifted to more positive values (+5‰ to +8 ‰ versus V-SMOW) indicative of the meteoric water interaction with the underlying evaporites and basaltic flows (Figure 7) (Table S-
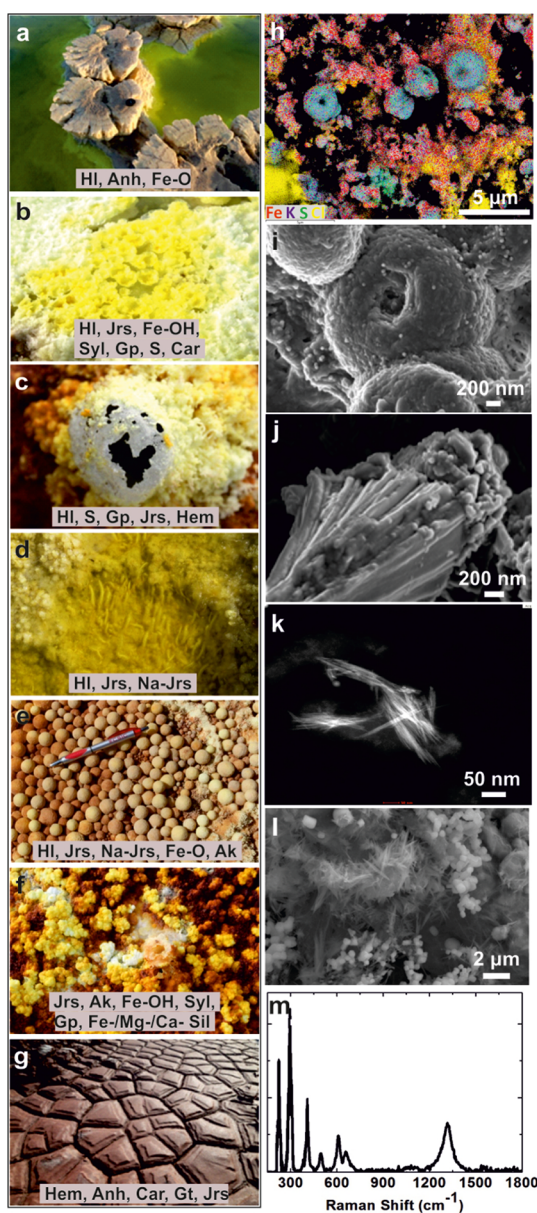
Figure 6. Pictures, microscopic images, and mineral composition of different Dallol patterns. (a) Water-lily structures created by subaqueous hydrothermal activity. (b) Halite flowers with variable degree of oxidation. (c) Halite with egg-like shapes forming around gas vents. (d) Twisted hollow tubes of halite. (e) Halite pearls. (f) Efflorescences. (g) Chocolate bar cracks formed during crystallization of an Fe-rich brine or melt. (h) FESEM and Fe, K, S, Cl EDX map of a jarosite-rich efflorescence. (i) FESEM image of jarosite spherules. (j) FESEM image of part of a jarosite spherule decorated by akaganeite particles. (k) TEM/HAADF image of the akaganeite nanoparticles. (l) hematite spindles. (m) Micro-Raman spectrum of the hematite spindles. Mineral abbr.: Hl=Halite, Jrs=Jarosite, Na-Jrs=Natrojarosite, Ak=Akaganeite, Gt=Goethite, Fe-OH=Fe-oxyhydroxides, Fe-O=Fe-oxides, Hem=Hematite, Syl=Sylvite, Gp=Gypsum, Anh=Anhydrite, Car=Carnallite, S=Sulfur, Fe-/Mg-/Ca-Sil=Fe-/Mg-/Ca-silicates.

3). The isotopic values of the pool water are both $\delta^{18}O$ and δD enriched as a result of the extreme evaporation rates of the pool water ($\delta^{18}O \sim 10.7‰$ and $\delta D > +3.2 ‰$). Note that the sample most affected by evaporation corresponds to the lowest, most acidic pool (BP1). Moreover, oxygen isotopic
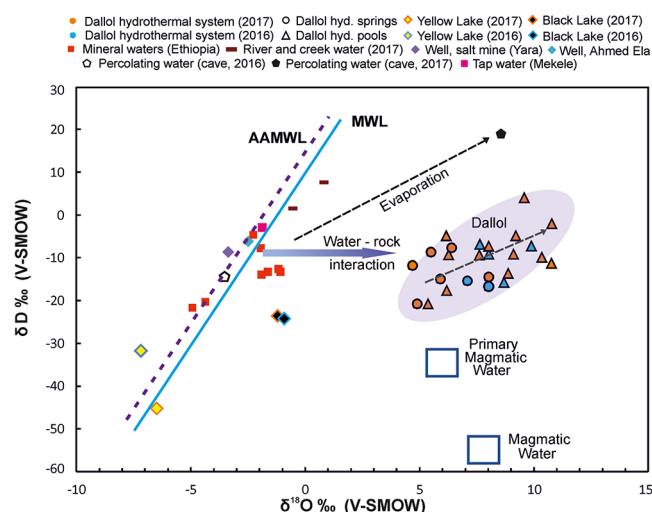
Figure 7. Stable isotope data for the Dallol hydrothermal brines and Black and Yellow Lake waters (2016 and 2017 campaigns). Dallol spring water has $\delta D‰$ values similar to the local meteoric water. The anomalous high $\delta^{18}O$ values of the hot springs indicate the interaction of the meteoric water with the underlying basaltic flows and evaporites. The $\delta^{18}O‰$ and δD values of the Dallol pools are higher due to evaporation processes ($\delta^{18}O > +10 ‰$, $\delta D > -10 ‰$). Yellow and Black Lake waters exhibit relatively negative values for both δD ($-25‰$ to $-48‰$) and $\delta^{18}O$ ($-1‰$ to $-7‰$) showing distinct hydrological processes with respect to the Dallol dome. MWL, Meteoric Water Line;[41] AAMWL, Addis Ababa Meteoric Water Line.[42] Magmatic and primary magmatic waters are plotted after refs 48−50.

values distinguish Dallol brines from the neighboring sites of Yellow and Black lakes, which exhibit relatively negative $\delta^{18}O$ values ($-1‰$ to $-7 ‰$), uncommon for the low latitude of the site[41] (Figure 7). This indicates different hydrological processes between the geothermal lakes and the system of the dome, that is also reflected in the difference in the hydrochemistry (see Introduction). As shown from other hyper-saline systems,[43,44] the negative δD values of Black and Yellow lakes can be a result of the very high salinity of these Mg−Ca−Cl-rich lakes that are under severe evaporation processes and exhibit complex evolution.

Concerning the dissolved gases of the hydrothermal brines of Dallol, the ratio N_2/Ar shows an excess of N_2 for the spring water indicative of the magmatic influence of the shallow source below the dome, whereas the slightly positive values measured at the pool water result from the subsequent water−atmosphere equilibration (see Supporting Information Table S-4).[45,46] For the free gases Darrah et al.,[13] reported more positive $\delta^{15}N$ values ($+2.93$ to $+4.5$) that were interpreted as a source of meta-sediment decomposition. This isotopic evolution of the free gases toward more negative values (see Table S-2) can be a result of the increased hydrothermal activity over the past years, as shown also from the 2016 and 2017 activity maps of the dome (Figure S-1).

The amount of organic matter in the dome is practically zero except for one spring system of gray color explored during the 2017 mission at the SW of the dome (Figure 1d). The gray color of that spring is owed to amorphous silica and degraded, partially graphitized, organic matter. The silica particles were identified by FESEM as remnants of partially dissolved diatom shells, whereas the measured $\delta^{13}C$ values of the organic matter ($-13‰$) are typical of marine algae.[47] Therefore, both silica

and organic matter are considered remnants of fossil diatoms trapped in the evaporitic sequence. For the detection of autotrophic and heterotrophic metabolic activity in the pools, we performed in situ incubations of isotopically labeled ^{18}O enriched water and urea-C,[13] respectively. Both incubations did not identify traces of biological activity (see Supporting Information, Figure S-3 and Table S-5). Likewise, no biologic material was detected during FESEM observation of fixed filters of Dallol brines and no organic compounds were picked up by Raman analysis of numerous efflorescences and precipitates (see Supporting Information Methods for sample preparation and fixation).

■ SUMMARY AND CONCLUSIONS

We report on a terrestrial hydrothermal system that discharges hyperacidic (near to zero pH and down to −1.7), hypersaline and oxygen-free brines that contain up to 150 g/L of iron. We demonstrate that the hyperacidic pH, the brine evolution, the color palette, and the mineral paragenesis are controlled by inorganic processes, related to iron oxidation and iron complexation with chlorides and sulfates. Our results suggest that life, if present, is not involved in the iron cycling and iron mineral precipitation at Dallol, as opposed to other submarine and terrestrial hydrothermal systems. Although it is well-known that life can tolerate or even thrive under extreme conditions,[51] the impact of multiple physicochemical extremes on microorganisms is poorly understood due to the scarcity of such polyextreme environments.[52] If microorganisms are present in Dallol polyextreme hydrothermal brines, their existence would expand the limit of life supporting habitance on Earth and on Earth-like planets, as we currently understand it, rendering Dallol a site of unique astrobiological significance.

At the same time, Dallol is a natural laboratory for the study of the precipitation of iron minerals and one of the very few present-day sites where we can witness the progressive oxidation of the iron formations as possibly occurred in early Earth, during the transition from anoxic-suboxic to oxygen-rich conditions.[53−56] Finally, the mineralogical prevalence of jarosite and related sulfates, and akaganeite and related Fe-oxyhydroxides in the precipitates of Dallol that have been also identified on different Martian geological sites,[57−59] the minor microbiologic and anthropogenic contamination of the dome, as well as, the intense iron corrosion, render Dallol a terrestrial Martian analogue-site of interest for future space missions.

■ ASSOCIATED CONTENT

ⓢ Supporting Information

TThe Supporting Information is available free of charge on the ACS Publications website at DOI: 10.1021/acsearthspace-chem.8b00141.

1. Supporting Methods. 1.1. The ferrozine (FZ) method for the Fe speciation in the liquids. 1.2. Isotopic analysis. 1.3. Biological sample preparation for the SEM study. 2. Supporting Results. 2.1. In situ incubations of urea-^{13}C and laboratory experiments. 3. Supporting Figures S-1 to S-3. 3.1. Figure S-1. Aerial photographs and related hydrothermal activity maps of Dallol dome for the 2016 and 2017 field campaigns. 3.2. Figure S-2. Fe species concentration for the spring water (S1) that is dominated by Fe(II) and four successive pools of Dallol (P1−P4) where Fe(III) is gradually increasing over Fe(II). 3.3. Figure S-3. $\delta^{13}C_{DIC}$ ‰ of isotopically labeled urea for incubations performed in situ and in the laboratory. 4. Supporting Tables S-1 to S-5. 4.1. Table S-1. Comparative chemical analysis of Dallol brines for the 2016 and 2017 field campaigns 4.2. Table S-2. Oxygen, nitrogen, argon, and carbon stable isotopes and atomic ratios in free gases from springs of Dallol and Black and Yellow Lake waters (sampling 2017). 4.3. Table S-3. Stable isotopes in H_2O and DIC (dissolved inorganic carbon) for Dallol hydrothermal brines compared to water from the wider area. 4.4. Table S-4. Oxygen, nitrogen, argon, and carbon stable isotopes and atomic ratios in dissolved gases from Dallol brines and Black and Yellow Lake waters. 4.5. Table S-5. First and second batch of measurements of $\delta^{13}C_{DIC}$‰ of isotopically labeled Urea for incubations performed in selected samples of Dallol pools and sterilized solutions of $FeCl_2$, $FeCl_3$, and $(NH_4)_2S_2O_8$ (PDF)

■ AUTHOR INFORMATION

Corresponding Author
*E-mail: jmgruiz@ugr.es.

ORCID 🅾
Electra Kotopoulou: 0000-0002-5789-846X
Juan Manuel Garcia-Ruiz: 0000-0002-4743-8718
Jose Maria Lopez-Garcia: 0000-0002-8564-9989

Author Contributions
E.K., A.D.H., J.M.L.G., and J.M.G.R. conducted the fieldwork and the sampling of the 2016 and 2017 missions. A.D.H. performed and analyzed the isotopic studies. J.M.D.V. designed and provided guidance for the UV−vis and Fe speciation study of the liquids. J.M.L.G. performed the geological mapping. F.R. provided guidance for the Raman study. I.G.T. conducted the scanning electron microscopy study. E.K. wrote the paper, performed the experiments, and analytical measurements and analyzed the data. J.M.G.R. designed the work and wrote the paper. All authors discussed and contributed to the last version of the manuscript.

Notes
The authors declare no competing financial interest.

■ REFERENCES

(1) Holwerda, J. G.; Hutchinson, R. W. Potash-bearing evaporites in the Danakil Region, Ethiopia. *Econ. Geol. Bull. Soc. Econ. Geol.* **1968**, 63, 124−150.

(2) Fazzini, M.; Bisci, C. The climate of Ethiopia. In *Landscapes and Landforms of Ethiopia*; Billi, P., Ed., World Geomorphological Landscapes; Springer, 2015.

(3) Berhanu, B.; Seleshi, Y.; Melesse, A. M. Surface water and groundwater resources of Ethiopia: Potentials and challenges of water resources development. In *Nile River Basin, Ecohydrological Challenges, Climate Change and Hydropolitics*; Melesse, A. M. et al., Eds.; Springer, 2014.

(4) Makris, J.; Ginzburg, A. The Afar depression: transition between continental rifting and sea-floor spreading. *Tectonophysics* 1987, *141*, 199–214.

(5) Prodehl, C. M.; et al. J. Crustal thinning in relationship to the evolution of the Afro-Arabian rift system: a review of seismic refraction data. *Tectonophysics* 1991, *198*, 311–327.

(6) Keir, D.; Bastow, I. D.; Pagli, C.; Chambers, E. L. The development of extension and magmatism in the Red Sea rift of Afar. *Tectonophysics* 2013, *607*, 98–114.

(7) Ebinger, C. J.; Casey, M. Continental breakup in magmatic provinces: An Ethiopian Example. *Geology* 2001, *29*, 527–530.

(8) Pérez, E.; Chebude, Y. Chemical analysis of Gaet'ale, a hypersaline pond in Danakil depression (Ethiopia): New record for the most saline water body on Earth. *Aquat. Geochem.* 2017, *23*, 109–117.

(9) Nobile, A.; Pagli, C.; Keir, D.; Wright, T. J.; Ayele, A.; Ruch, J.; Acocella, V. Dike-fault interaction during the 2004 Dallol intrusion at the northern edge of the Erta Ale Ridge (Afar, Ethiopia). *Geophys. Res. Lett.* 2012, *39*, L19305 1-6 p.

(10) Pagli, C.; Wright, T. J.; Ebinger, C. J.; Yun, S.-H.; Cann, J. R.; Barnie, T.; Ayele, A. Shallow axial magma chamber at the slow-spreading Erta Ale Ridge. *Nat. Geosci.* 2012, *5*, 284–288.

(11) Hovland, M.; Rueslåtten, H. G.; Johnsen, H. K.; Kvamme, B.; Kuznetsova, T. Salt formation associated with sub-surface boiling and supercritical water. *Mar. Pet. Geol.* 2006, *23*, 855–869.

(12) Carniel, R.; Jolis, E. M.; Jones, J. A geophysical multi-parametric analysis of hydrothermal activity at Dallol, Ethiopia. *J. Afr. Earth Sci.* 2010, *58*, 812–819.

(13) Darrah, T. H.; Tedesco, D.; Tassi, F.; Vaselli, O.; Cuoco, E.; Poreda, R. J. Gas chemistry of the Dallol region of the Danakil Depression in the Afar region of the northern-most East African Rift. *Chem. Geol.* 2013, *339*, 16–29.

(14) Bonatti, E.; Fisher, D. E.; Joensuu, O.; Rydell, H. S.; Beyth, M. Iron-Manganese-Barium Deposit from the Northern Afar Rift (Ethiopia). *Econ. Geol. Bull. Soc. Econ. Geol.* 1972, *67*, 717–730.

(15) Sharp, Z. D.; Atudorei, V.; Durakiewicz, T. A rapid method for determination of hydrogen and oxygen isotope ratios from water and hydrous minerals. *Chem. Geol.* 2001, *178*, 197–210.

(16) Delmelle, P.; Bernard, A. Downstream composition changes of acidic volcanic waters discharged into the Banyupahit stream, Ijen caldera, Indonesia. *J. Volcanol. Geotherm. Res.* 2000, *97*, 55–75.

(17) Rowe, G. L.; Brantley, S. L.; Fernandez, M.; Fernandez, J. F.; Borgia, A.; Barquero, J. Fluid-volcano interaction in an active stratovolcano: the crater lake system of Poás volcano, Costa Rica. *J. Volcanol. Geotherm. Res.* 1992, *49*, 23–51.

(18) Rodríguez, A.; van Bergen, M. J. Superficial alteration mineralogy in active volcanic systems: An example of Poás volcano, Costa Rica. *J. Volcanol. Geotherm. Res.* 2017, *346*, 54–80.

(19) Kalacheva, E.; Taran, Y.; Kotenko, T.; Hattori, K.; Kotenko, L.; Solis-Pichardo, G. Volcano–hydrothermal system of Ebeko volcano, Paramushir, Kuril Islands: Geochemistry and solute fluxes of magmatic chlorine and sulfur. *J. Volcanol. Geotherm. Res.* 2016, *310*, 118–131.

(20) Rodríguez, A.; Varekamp, J. C.; van Bergen, M. J.; Kading, T. J.; Oonk, P. B. H.; Gammons, C. H.; Gilmore, M. In *Copahue Volcano*; Tassi, F.; Vaselli, O.; Caselli, A., Eds.; Springer-Verlag: Berlin, Heidelberg, 2015; pp 141–172.

(21) Agusto, M. R.; Caselli, A.; Daga, R.; Varekamp, J.; Trinelli, A.; Dos Santos Afonso, M.; Velez, M. L.; Euillades, P.; Ribeiro Guevara, S. The crater lake of Copahue volcano (Argentina): geochemical and thermal changes between 1995 and 2015. In *Geochemistry and Geophysics of Active Volcanic Lakes*; Ohba, T., Capaccioni, B., Caudron, C., Eds.; Geological Society, London, Special Publications, 2016; Vol. *437*; pp 107–130.

(22) Varekamp, J. C.; Ouimette, A. P.; Herman, S. W.; Flynn, K. S.; Bermudez, A.; Delpino, D. Naturally acid waters from Copahue volcano, Argentina. *Appl. Geochem.* 2009, *24*, 208–220.

(23) Christenson, B. W.; Wood, C. P. Evolution of a vent-hosted hydrothermal system beneath Ruapehu Crater Lake, New Zealand. *Bull. Volcanol.* 1993, *55*, 547–565.

(24) Inguaggiato, C.; Censi, P.; Zuddas, P.; Londoño, J. M.; Chacón, Z.; Alzate, D.; Brusca, L.; D'Alessandro, W. Geochemistry of REE, Zr and Hf in a wide range of pH and water composition: The Nevado del Ruiz volcano-hydrothermal system (Colombia). *Chem. Geol.* 2015, *417*, 125–133.

(25) Colvin, A.; Rose, W. I.; Varekamp, J. C.; Palma, J. L.; Escobar, D.; Gutierrez, E.; Montalvo, F.; Maclean, A.: Crater lake evolution at Santa Ana Volcano (El Salvador) following the 2005 eruption. In *Understanding open-vent volcanism and related hazards: Geological Society of America Special Paper 498*; Rose, W. I., Palma, J. L., Delgado Granados, H., Varley, N., Eds.; Geological Society of America, 2013; pp 23–43.

(26) Fernández-Remolar, D. C.; Morris, R. V.; Gruener, J. E.; Amils, R.; Knoll, A. H. The Río Tinto Basin, Spain: Mineralogy, sedimentary geobiology, and implications for interpretation of outcrop rocks at Meridiani Planum, Mars. *Earth Planet. Sci. Lett.* 2005, *240*, 149–167.

(27) Nordstrom, D. K.; Alpers, C. N.; Ptacek, K. J.; Blowes, D. W. Negative pH and Extremely Acidic Mine Waters from Iron Mountain, California. *Environ. Sci. Technol.* 2000, *34*, 254–258.

(28) Craig, H.: Geochemistry and origin of the Red Sea brines. In *Hot brines and recent heavy metal deposits in the Red Sea, A geochemical and geophysical acoount*; Degens, E. T., Ross, D. A., Eds.; Springer: Berlin, Heidelberg, 1969; pp 208–242.

(29) Warren, J. K. Danakil Potash, Ethiopia: Beds of Kainite-Carnallite, Part 2 of 4, 2015. SaltWork Consultants Pte Ltd: Kingston Park, Adelaide.

(30) Millero, F. J. The thermodynamics and kinetics of the hydrogen sulfide system in natural waters. *Mar. Chem.* 1986, *18*, 121–147.

(31) Ohmoto, H.; Lasaga, A. C. Kinetics of reactions between aqueous sulfates and sulfides in hydrothermal systems. *Geochim. Cosmochim. Acta* 1982, *46*, 1727–1745.

(32) Pittwell, L. R. Some coordination effects in natural waters of Ethiopia. *J. Hydrol.* 1972, *17*, 225–228.

(33) Rudolph, W.; Brooker, M. H.; Tremaine, P. R. Raman spectroscopic investigation of aqueous $FeSO_4$ in neutral and acidic solutions from 25 to 303 C inner and outer-sphere complexes. *J. Solution Chem.* 1997, *26*, 757–767.

(34) Rull, F.; Sobrón, F. Band profile analysis of the Raman spectra of sulphate ions in aqueous solutions. *J. Raman Spectrosc.* 1994, *25*, 693–698.

(35) Heinrich, C. A.; Seward, T. M. A spectrophotometric study of aqueous iron (II) chloride complexing from 25 to 200°C. *Geochim. Cosmochim. Acta* 1990, *54*, 2207–2221.

(36) Stefánsson, A.; Seward, T. M. A spectrophotometric study of iron(III) hydrolysis in aqueous solutions to 200 °C. *Chem. Geol.* 2008, *249*, 227–235.

(37) Kanno, H.; Hiraishi, J. A Raman study of aqueous solutions of ferric nitrate, ferrous chloride and ferric chloride in the glassy state. *J. Raman Spectrosc.* 1982, *12*, 224–227.

(38) Koyama, Y.; Umemoto, Y.; Akamatsu, A.; Uehara, K.; Tanaka, M. Raman spectra of chrolophyll forms. *J. Mol. Struct.* 1986, *146*, 273–287.

(39) Withnall, R.; Chowdhry, B. Z.; Edwards, S. J.; et al. Raman spectra of carotenoids in natural products. *Spectrochim. Acta, Part A* 2003, *59*, 2207–2212.

(40) Nugent, P. W.; Shaw, J. A.; Vollmer, M. Colors of thermal pools at Yellowstone National Park. *Appl. Opt.* 2015, *54*, B128–139.

(41) Craig, H. Isotopic variations in meteoric waters. *Science* 1961, *133*, 1702–1703.

(42) Craig, H.; et al. *Geochemistry and Hydrology of Geothermal Waters in the Ethiopian Rift Valley*; California, San Diego, 1977.

(43) Sofer, Z.; Gat, J. The isotope composition of evaporating brines: effect of the isotopic activity ratio in saline solutions. *Earth Planet. Sci. Lett.* **1975**, *26*, 179−186.

(44) Oerter, E. J.; Singleton, M.; Davisson, M. L. Hydrogen and oxygen stable isotope dynamics of hyper-saline and salt-saturated aqueous solutions. *Geochim. Cosmochim. Acta* **2018**, *238*, 316−328.

(45) Snyder, G.; Poreda, R.; Fehn, U.; Hunt, A. Sources of nitrogen and methane in Central American geothermal settings: Noble gas and 129I evidence for crustal and magmatic volatile components. *Geochem., Geophys., Geosyst.* **2003**, *4*, 1−28.

(46) Kyser, T. K. Stable isotope variations in the mantle. *Reviews in Mineralogy and Geochemistry* **1986**, *16*, 141−164.

(47) Raven, J. A.; Walker, D. I.; Johnston, A. M.; Handley, L. L.; et al. Implications of ^{13}C natural abundance measurements for photosynthetic performance by marine macrophytes in their natural environment. *Mar. Ecol.: Prog. Ser.* **1995**, *123*, 193−205.

(48) Sheppard, S. M.; Nielsen, R. L.; Taylor, H. P. Hydrogen and oxygen isotope ratios in minerals from porphyry copper deposits. *Econ. Geol. Bull. Soc. Econ. Geol.* **1971**, *66*, 515−542.

(49) Sheppard, S. M. F. Characterization and Isotopic Variations in natural waters. *Reviews in Minerology* **1986**, *16*, 165−183.

(50) Rye, R. O.; O'Neil, J. R. The ^{18}O content of water in primary fluid inclusions from Providencia, north-central Mexico. *Econ. Geol.* **1968**, *63*, 232−238.

(51) Rothschild, L. J.; Mancinelli, R. L. Life in extreme environments. *Nature* **2001**, *409*, 1092−1101.

(52) Harrison, J. P.; Gheeraert, N.; Tsigelnitskiy, D.; Cockell, C. S. The limits for life under multiple extremes. *Trends Microbiol.* **2013**, *21*, 204−212.

(53) Bekker, A.; Holland, H. D.; Wang, P. L.; Rumble, D., Iii; Stein, H. J.; Hannah, J. L.; Coetzee, L. L.; Beukes, N. J. Dating the rise of atmospheric oxygen. *Nature* **2004**, *427*, 117.

(54) Lyons, T. W.; Reinhard, C. T.; Planavsky, N. J. The rise of oxygen in Earth's early ocean and atmosphere. *Nature* **2014**, *506*, 307−315.

(55) Halevy, I.; Alesker, M.; Schuster, E. M.; Popovitz-Biro, R.; Feldman, Y. A key role for green rust in the Precambrian oceans and the genesis of iron formations. *Nat. Geosci.* **2017**, *10*, 135−139.

(56) Canfield, D. E. The early history of atmospheric oxygen: Homage to Robert M. Garrels. *Annu. Rev. Earth Planet. Sci.* **2005**, *33*, 1−36.

(57) Klingelhofer, G.; Morris, R. V.; Bernhardt, B.; Schroder, C.; Rodionov, D. S.; de Souza, P. A., Jr.; Yen, A.; Gellert, R.; Evlanov, E. N.; Zubkov, B.; Foh, J.; Bonnes, U.; Kankeleit, E.; Gutlich, P.; Ming, D. W.; Renz, F.; Wdowiak, T.; Squyres, S. W.; Arvidson, R. E. Jarosite and hematite at Meridiani Planum from Opportunity's Mössbauer Spectrometer. *Science* **2004**, *306*, 1740−1745.

(58) Amils, R.; Fernandez-Remolar, D.; et al. Rio Tinto: a geochemical and mineralogical terrestrial analogue of Mars. *Life (Basel, Switz.)* **2014**, *4*, 511−534.

(59) Bishop, J. L.; Murad, E.; Dyar, M. D. Akaganeite and schwertmannite: Spectral properties and geochemical implications of their possible presence on Mars. *Am. Mineral.* **2015**, *100*, 738−746.